

## Simple test with rotation curves for the multistate scalar field dark matter model

Jordi Solís-López,<sup>1</sup> Luis E. Padilla<sup>2,\*</sup> and Tonatiuh Matos<sup>1</sup>

<sup>1</sup>*Departamento de Física, Centro de Investigación y de Estudios Avanzados del IPN, A.P. 14-740, 07000 México D.F., México*

<sup>2</sup>*Astronomy Unit, Queen Mary University of London, Mile End Road, London, E1 4NS, UK*



(Received 14 January 2024; accepted 26 March 2024; published 29 April 2024)

We use the concept of coadded rotation curves of Salucci *et al.* to investigate the properties of axisymmetric multistate scalar field dark matter (SFDM) halos in low surface brightness (LSB) galaxies and dwarf disc galaxies. To this end, we expand the wave function of the scalar field into its multistates and solve the field equations numerically. We fit their rotation curves in two-state configurations finding that a two-state configuration fits better than the single ground-state (soliton) configuration in the dwarf disc and in the smaller of the LSB galaxies. We obtain a SFDM mass  $\mu = 2.38 \pm 0.12 \times 10^{-23}$  eV/ $c^2$  for the dwarf disc galaxies and  $\mu = 1.05 \pm 0.14 \times 10^{-23}$  eV/ $c^2$  for the smaller of the LSB galaxies. For the larger of the LSB galaxies a mass of the order of  $\mu = O(10^{-24}) - O(10^{-25})$  eV/ $c^2$  is obtained, where the mass  $\mu$  is the effective mass measured by an outside observer due to the finite temperature of the SFDM in the galaxy.

DOI: [10.1103/PhysRevD.109.083034](https://doi.org/10.1103/PhysRevD.109.083034)

### I. INTRODUCTION

It is now well accepted that to understand how galaxies and clusters of galaxies were formed, in addition to the baryonic matter, which is responsible for contributing to the gravitational pull necessary to maintain stable all these structures in the Universe, it is necessary to introduce an extra element known as dark matter. It is also well known that without this dark matter component, it is difficult to explain the observed anisotropies in the cosmic microwave background radiation, the large-scale structure formation in the Universe, the galactic formation process, or the gravitational lenses of distant objects, among others. In this way, today, it is well established that dark matter is a fundamental ingredient of the cosmic inventory.

In this direction, the standard cosmological model assumes that the dark matter of the Universe is comprised of a nonrelativistic, collisionless gas—cold dark matter (CDM)—and usually assumed to be weakly interacting massive particles (WIMPs) which originated as a thermal relic of the Big Bang [1,2]. Although WIMP dark matter describes observations well at cosmological scales, it is in apparent conflict with some observations on small scales [e.g., the problem of cuspy-core halo density profiles, overproduction of satellite dwarfs within the local group, and others; see, for example, [3–7]]. All of these discrepancies are based on the fact that from CDM  $N$ -body simulations of structure formation, the CDM clusters form halos with a universal Navarro-Frenk-White (NFW)

density profile at all scales [8], which is proportional to  $r^{-1}$  (a ‘cuspy’ profile) at small radii, whereas it decays as  $r^{-3}$  for large radii. Furthermore, the attempts to detect WIMPs directly or indirectly [9] have no successful results, and a large range of parameters thought to be detectable has not been measured. To help us solve all these issues several alternative dark matter models have been proposed.

One of the strongest candidates to substitute the standard CDM is the scalar field dark matter (SFDM) model. This model states that dark matter is an ultralight real or complex scalar field, minimally coupled to gravity, and interacting only gravitationally with baryonic matter. The main idea was originated about two decades ago by [10–16] and [17], with some hints traced further back in [18,19]. However, it was systematically studied for the first time by [20,21] [for a review of SFDM, see [22–26]] and [27] for a current review.

Over the years, the idea has been rediscovered or renamed by various authors, the most popular names being SFDM [10], wave dark matter [28], fuzzy dark matter [14], Bose-Einstein condensate dark matter [29], and ultralight axion dark matter [30,31]. In this work, we use the most general name SFDM.

The SFDM model alleviates problems at small scales because of the dynamical properties derived from its macroscopic-sized de Broglie wavelength. It solves the cusp/core problem in CDM as seen in several cosmological simulations of structure formation [28,32–36] in which the SFDM halos have cored density profiles within their inner most regions of galactic systems. These halos have a central core [referred to in the literature as solitons[36–39]] and

\*Corresponding author: [lepadilla@icf.unam.mx](mailto:lepadilla@icf.unam.mx)

are surrounded by an envelope generated by a quantum interference pattern that is well fitted by an NFW density profile.

Solitons have a size of similar magnitude to the de Broglie wavelength of individual bosons:

$$\lambda_{\text{dB}} \propto (\mu_0 v)^{-1},$$

where  $v$  is the “average virial velocity” of the bosons and  $\mu_0$  its mass, that, to reproduce galactic cores of one kiloparsec of size, is typically assumed in the range of  $\mu_0 \sim (10^{-20} - 10^{-22}) \text{ eV}/c^2$ .

In different simulations, a strong scaling correlation has been found between the mass  $M_c$  of the core and the mass  $M_h$  of the whole halo given by  $M_c \propto M_h^\beta$ .<sup>1</sup> The particular value of the  $\beta$  parameter is still under debate given that different authors have obtained different results. The value  $\beta = 1/3$  was found in [28,32] from their fully cosmological simulations. And  $\beta = 5/9$  by [35,42] adopting more simplified scenarios on galaxy formation but with better resolution. It was thanks to this scaling relation that has been proposed in [41] [see also [43]] that these soliton profiles could be also responsible for explaining the presence of supermassive black holes at galactic nuclei in the most massive galaxies. On the other hand, there have been some other works that have tried to fix this  $\beta$  parameter but have not succeeded, since, they affirm, that the results of their simulations were not consistent with a single value of  $\beta$  for all their simulated galaxies. The latter is consistent with the results presented in [44], in which the authors studied the scaling relations for SFDM halos. In that work, the authors used a modified version of the GADGET code (AX-gadget) to study how the different scaling relations for cores and envelopes in the SFDM are modified once incorporating the different effects that are added once studying galaxies in a real cosmological environment. Their results showed that not all galaxies can be described with a single  $\beta$  and the scaling relations reported by [28,32,35] and [42] are only consistent with galaxies in some limiting cases, being only valid for the most relaxed and spherical symmetric systems.

Due to the discrepancy of  $\beta$  in the core-halo mass relation, it is clear that this topic is not yet closed. In this direction, it has been a related idea that was proposed for the first time in [45] in which the gravitational coexistence of different energy eigenstates of the wave function (multistates) are responsible for describing a complete galaxy in this SFDM scenario. Recently, in [46] they showed a general method to find solutions of multistate configurations. This method encompasses the spherical multistates of [47], excited single states, l-boson stars [48] as well as the

<sup>1</sup>We recommend [40] for the extension of this core-halo mass relation in the presence of baryonic components or [41] when a self interaction between the SFDM particles is allowed.

new axisymmetric multistates, furthermore, they show a possible formation process of these axisymmetric configurations by the collision of single states. Although they do not give a bound, they show that the particular solutions they consider are stable. The possibility of multistates is still in its infancy, as the scientific community is just beginning to study this scenario.

The idea of introducing these multistate configurations, which we take as our work proposal, is the following: For an expanding universe, the scalar field cools down due to its expansion. After a while, this causes the scalar field, the boson gas, to freeze and condense. For an ideal boson gas, the condensation temperature goes like  $T_c \sim \mu_0^{-5/3}$ , implying that if the mass of the scalar field is big, the condensation temperature is small, but if the mass is light, or ultralight, the condensation temperature could be very high. However, after the turnaround, galaxies start to form and recollapse, increasing the temperature of the bosons again. Depending on the initial conditions of the galaxy formation, the boson particles can reach excited states, although most of the boson particles remain in the condensate state, i.e. the ground state.

These excited particles can be interpreted as other scalar fields. Thus, if after its formation a galaxy contains boson particles in several quantum states, this can be seen as a galaxy with different scalar fields, too. In this case, the scalar field can be seen as living in a thermal bath, where the Klein-Gordon equation is modified as  $\square\Phi - dV/d\Phi = 0$ , where the scalar field potential  $V(\Phi)$  is

$$V(\Phi) = -\frac{\mu_0^2 c^2}{\hbar^2} |\Phi|^2 + \frac{1}{2} \Lambda |\Phi|^4 + \frac{1}{4} k_B^2 T^2 |\Phi|^2 - \frac{\pi^2 k_B^2}{90 \hbar^2 c^2} T^4. \quad (1)$$

In the above expression,  $k_B$  is the Boltzmann’s constant and  $T$  the thermal bath temperature (see for example [49,50]). With this scalar field potential, the system experiments a symmetry breakdown at the critical temperature  $k_B T_c = 2\mu_0 c^2 / \sqrt{\Lambda}$ . In our case, the mass  $\mu_0$  is ultralight, but the self-interaction parameter  $\Lambda$  is also very small,<sup>2</sup> several orders of magnitude smaller than the mass. When the scalar field reaches temperatures enough below this one, the system condensates [54]. This transforms the dispersion relation of the Klein-Gordon equation into (see [55,56])

<sup>2</sup>It is worth mentioning that the  $T = 0 = \Lambda$  case is the most widely studied since it takes the minimum necessary considerations to have an ultralight scalar field as a candidate for dark matter, which is why we intend to take this model as a workhorse for our work, by considering a finite temperature-dependent mass of the galactic halo (see main text). The case with  $T = 0$  and  $\Lambda \neq 0$  has also been widely studied in the literature, where it has been shown that said self-interaction term can have important consequences at the cosmological level (see for example [51–53]).

$$\omega^2 = k^2 c^2 + \frac{2\mu_0^2 c^4}{\hbar^2} \left(1 - \frac{T^2}{T_c^2}\right) \quad (2)$$

where  $\omega$  is the frequency associated with the kinetic energy of the scalar field and  $k$  is its wave number. The critical temperature of condensation is very high because it is inversely proportional to the mass of the scalar field  $T_c \sim \mu_0^{-5/3}$ . But the critical temperature of symmetry breaking is higher than the critical temperature of condensation  $T_c > T_c$  [54]. This means that the scalar field breaks its symmetry and after that condensates. After condensation, the scalar field starts a process of gravitational cooling and forms stable objects that we see as the halo of galaxies. The important term here is the second one on the right-hand side because Eq. (2) can be written as  $\omega^2 = k^2 c^2 + \mu^2 c^2$ , defining  $\mu = \mu_0 c / \hbar \sqrt{1 - T^2/T_c^2}$ . It follows that, if the scalar field collapses into a halo, and its final temperature is bigger than the cosmological average temperature, the system effectively sees a smaller mass  $\mu$ , even when the mass  $\mu_0$  is constant. We explain these results using an example. Cosmological observations have constrained the mass of the SFDM using the Ly- $\alpha$  observations such that the scalar field mass should be  $\mu_0 \sim 10^{-21}$  eV [57]. Now let us suppose that during its collapse the halo of a galaxy reaches the thermal bath temperature  $T \sim 0.9999995 T_c$ , then the effective mass becomes  $\mu = 10^{-24}$  eV. Observe that the real mass of the scalar field remains to be  $10^{-21}$  eV, but all the phenomena in the galaxy can be explained using the value  $10^{-24}$  eV. Of course, a galaxy with this temperature contains most of the particles in the ground state, but a great amount of them are now in excited states. If the scalar field collapses into a halo where its temperature is similar to the average cosmological temperature, the system sees effectively a mass close to  $\mu_0$ . On the other hand, we expect that small galaxies contain the ground state and maybe one excited state, while the big galaxies contain several excited states. Therefore, we expect that the scalar field in big galaxies is warmer and the system sees a smaller effective mass of the scalar field than in small galaxies, where the effective mass could be bigger, but always smaller than for cosmological constrictions. We then expect that the effective mass of the scalar field in each galaxy depends on its final temperature of collapse, which determines its size and properties. In other words, the thermal bath will cause the SFDM halo of the galaxy not to remain any more in the ground state; it will be a part of the bosons that emigrate to different excited states. Therefore we plan here to work with multistate SFDM.

Our intention in this work is to test multistate SFDM profiles with rotation curves. In Ref. [58], it was demonstrated that excited states are stable systems as long as the ground state solution is included in the multistate configuration. Specifically, when excited states exist independently, without the presence of the ground state,

they tend to relax towards it. However, when the ground state is incorporated into the multistate configuration, these composite systems exhibit remarkable stability over extended periods. Such stability is adequate for elucidating the presence of a galaxy's halo, incorporating contributions from both states. For this purpose, we decided to use the so-called universal rotation curve (URC) method, which was introduced in [59,60] for the case of spiral galaxies, but it has also been applied to low surface brightness (LSB) galaxies [61], dwarf disc galaxies [62] and LSB and dwarf disc combined [63]. The URC is the model that fits the coadded rotation curve, which is constructed from a sample of rotation curves with normalized radii and normalized circular velocities. The URC thus is a function with two parameters: the normalized radial coordinate and a galaxy family identifier that could be, for example, the optical velocity  $v_{\text{opt}} = v(R_{\text{opt}})$  (measured velocity at the optical radius  $R_{\text{opt}}$ , the radius of the sphere encompassing 83% of the luminous matter), galaxy luminosity  $L_B$ , or absolute magnitude  $M_K$ . The great advantage of using URCs is that once we have found a good mass model for the coadded rotation curve, it is possible to recover the mass model of each galaxy within that particular family.

The article is organized as follows: In Sec. II we present the multistate scalar field dark matter (multiSFDM) model, the background, the properties, and the particular configurations we will use in the paper. In Sec. III B 1 we present the mass model for the dwarf disc galaxies, in Sec. III B 2 the mass model for the LSB galaxies, in Sec. IV the discussion of the results, and finally in Sec. V we give our conclusions.

## II. THE SCALAR FIELD DARK MATTER MODEL

In what follows we will assume that the scalar field is at a temperature different from zero, which allows the scalar field to be in different excited states. Therefore, we can expand the scalar field in these multistate configurations. We solve the equations for self-gravitating scalar fields  $\Psi$  of effective mass  $\mu$  that play the field theory version of spinless particles coupled to Einstein's gravity in the weak field and nonrelativistic regimes: the three-dimensional Gross-Pitaevskii-Poisson system, which in the case where there is no self interaction, becomes the Schrödinger-Poisson system [47]:

$$i\hbar \frac{\partial \Psi_{nlm}}{\partial t} = -\frac{\hbar^2}{2\mu} \nabla^2 \Psi_{nlm} + \mu V \Psi_{nlm},$$

$$\nabla^2 V = 4\pi G \sum_{nlm} |\Psi_{nlm}|^2$$

where  $\Psi_{nlm}(\vec{x}, t)$  is the wave function in the state labeled by  $(n, l, m)$ ,  $V(\vec{x}, t)$  is the self-gravitational potential (the potential produced by the dark matter density  $\sum |\Psi_{nlm}|^2$ ),

and  $G$  is the gravitational constant. The ground state is found when  $n = 1, l, m = 0$ .

If we consider stationary states,  $\Psi_{nlm}(t, r, \theta, \varphi) = \frac{\hat{\mu}c}{\sqrt{4\pi G}} e^{iE_{nlm}t/\hbar} \Phi_{nlm}(r, \theta, \phi)$ , it becomes

$$\hat{\nabla}^2 \Phi_{nlm} - 2(\hat{V} + \hat{E}_{nlm})\Phi_{nlm} = 0, \quad (3a)$$

$$\hat{\nabla}^2 \hat{V} = \sum_{nlm} |\Phi_{nlm}|^2, \quad (3b)$$

where  $c$  is the speed of light,  $\hbar$  is the reduced Planck constant,  $\hat{V} \equiv V/c^2$ ,  $\hat{E}_{nlm} \equiv \frac{E_{nlm}}{\mu c^2}$ , and  $\hat{\mu} \equiv \mu c/\hbar$  has units of length<sup>-1</sup> and makes the coordinates and the Laplace operator dimensionless:  $\hat{r} = \hat{\mu}r$  and  $\hat{\nabla}^2 = \frac{1}{\hat{r}^2} \nabla^2$ .

The Schrödinger-Poisson system has the scaling property

$$(\hat{r}, \Phi_{nlm}, \hat{V}, \hat{E}_{nlm}, N) \rightarrow (\hat{r}/\sqrt{\lambda}, \lambda \Phi_{nlm}, \lambda \hat{V}, \lambda \hat{E}_{nlm}, \sqrt{\lambda} N) \quad (4)$$

that give us two free parameters for our model, the particle effective mass  $\mu$  and the scaling parameter  $\lambda$ .<sup>3</sup> Using this  $\lambda$  parameter, it is possible to construct an infinite number of solutions of the Schrödinger-Poisson system once one solution is known.

In what follows, we work with dimensionless variables and we will drop the  $\hat{\phantom{x}}$  symbol for simplicity,<sup>4</sup> and only when dimensional variables are used in the figures, the units will be stated.

We can consider several cases for a dark matter halo: (a) The simplest possibility is to consider a single state, when all boson particles are in the same state  $\Psi_{nlm}$ , with  $n$  taking only one value 1,2,..., and also for  $l$  and  $m$  taking one of its possible values  $l = 0, 1, \dots, n-1$  and  $m = -l, -l+1, \dots, l$ . In this case, there is only one Schrodinger equation (3a) and only one term in the right-hand side of Eq. (3b). It happens that in the single state case only the ground state  $\Psi_{100}$  is stable [64]. Additionally, it has been also shown that arbitrary and isolated configurations relax through gravitational cooling to the ground state [65,66].

One other possibility is (b) multistates (multiSFDM), states where some particles are in the ground state and some in other excited states. The dark matter density in the right-hand side of Eq. (3b) is then of the form  $|\Psi_{100}|^2 + |\Psi_{nlm}|^2$ ,  $n = 2, 3, \dots$ ;  $l = 0, 1, \dots, n-1$ ;

<sup>3</sup>Whenever more states are considered, extra free parameters appear, those could be, for example, the ratio between wave function amplitudes  $\zeta \equiv \frac{\Psi_{100}}{\Psi_{nlm}}$ .

<sup>4</sup>To return to the dimensional variables is necessary to multiply the dimensionless variable by  $\mu$  and the universal constants (as conveniently). Once the scaling parameter is established it is also necessary to multiply (as conveniently) the variables by  $\lambda$ . For example  $\hat{r} \rightarrow r = \hat{r}\hat{\mu}^{-1}\lambda^{-1/2}$ .

$m = -l, -l+1, \dots, l$ , and there is one Schrödinger equation (3a) for each state. The idea is that a galaxy should be described with a collection of states. The particular value of the  $n, l, m$  parameters should depend on the process of evolution and formation of the galaxy we are interested in modeling, so in general these parameters should not be able to be set in a general way for all types of galaxies.

However, as an example and to show the enormous advantages that these multistate configurations give us, in this work we will adopt working with scenarios of only two states, that is, we will take the ground state together with one excited state of the previous system.<sup>5</sup> Particularly, we shall only concentrate on the multistate configurations that we present in what follows, to say, we shall work with the multistate configurations (100, 21m) and (100,200), which turn out to be the first excited states. Of course, our choice to work with these configurations is very simplistic since, in general, one would expect that a system of only two states (a ground state and an excited state) should not be sufficient to describe the entire range of masses for galaxies that exist in the Universe, however, to compensate for this lack of multistates we will allow the mass of the scalar field to acquire smaller values as the masses of the galaxies are more massive (a greater number of multistates should translate into an effective lower mass for the scalar field, as explained in the Introduction, but never smaller than the value provided by cosmological constrictions).

### A. multiSFDM case (100, 21m)

Following the general framework of [46] for the multiSFDM case ( $\Psi_{100}, \Psi_{21m}$ ), the system (3) becomes

$$\begin{aligned} \nabla_{r_0}^2 \psi_{100}(r) &= 2(V_{00} - E_{100})\psi_{100}, \\ \nabla_{r_1}^2 \psi_{21m}(r) &= 2(V_{00} + Cr^2V_{20} - E_{21m})\psi_{21m}, \\ \nabla_{r_0}^2 V_{00}(r) &= \psi_{100}^2 + r^2\psi_{21m}^2, \\ \nabla_{r_2}^2 V_{20}(r) &= |C|\psi_{21m}^2, \end{aligned} \quad (5)$$

where we have expanded the gravitational potential in spherical harmonics  $Y_{lm}(\theta, \phi)$  as

$$V(r, \theta) = \sqrt{4\pi}(V_{00}(r)Y_{00}(\theta, \phi) + V_{20}(r)r^2Y_{20}(\theta, \phi))$$

and the scalar field states have been written as  $\Phi_{nlm} = \psi_{nlm}(r)r^l Y_{lm}(\theta, \phi)$ . The constant  $C = 2/\sqrt{5}$  for  $m = 0$  and  $C = -1/\sqrt{5}$  for  $m = \pm 1$ . The  $l$ -laplacian operator is defined as

$$\nabla_{r_l}^2 \equiv \frac{\partial^2}{\partial r^2} + \frac{2(l+1)}{r} \frac{\partial}{\partial r}.$$

<sup>5</sup>The idea of using in all cases the ground state is because it has been demonstrated that for multistate configurations to be stable, the ground state must be presented in the system [47].

The enclosed mass at radius  $r$  of the dark matter halo is

$$M(r) = \frac{c^2}{G\tilde{\mu}} N(r)$$

with  $N = \sum_{n,l,m} N_{nlm}$  the dimensionless enclosed mass.<sup>6</sup> Here, the number of particles  $N_{nlm}$  of each state is

$$N_{nlm} = \int |\Phi_{nlm}|^2 r^2 dr d\Omega.$$

The circular velocity of a particle due to this SFDM halo is given by<sup>7</sup>

$$v_h^2 = \frac{P_0}{r} - \frac{\sqrt{5}}{2} r^2 (rP_2 + 2V_{20}) \quad (6)$$

where

$$P_0 = r^2 \frac{dV_{00}}{dr}, \quad P_2 = \frac{dV_{20}}{dr}.$$

The system (5) with the following boundary conditions

$$\begin{aligned} \psi_{100}(r_f) &= 0, & \left. \frac{d\psi_{100}}{dr} \right|_{r=0} &= 0, \\ \psi_{21m}(r_f) &= 0, & \left. \frac{d\psi_{21m}}{dr} \right|_{r=0} &= 0, \\ V_{00}(r_f) &= -\frac{N_T}{r_f}, & P_0(r_f) &= N_T, \\ V_{20}(r_f) &= 0, & P_2(0) &= 0, \end{aligned}$$

becomes a boundary value problem that is solved using the shooting method. Here  $N_T$  is the total mass enclosed by the boundary radius  $r = r_f$ ,  $N_T = N(r_f)$ . Although solutions can be found for  $m = 0$  and  $m = 1$ , in this study we simplify our description and work only with the case  $m = 0$ .

We fix the central value  $\psi_{100}(0) = 1$  to find the eigenvalues  $E_{100}$  and  $E_{210}$  and the initial values  $V_{00}(0)$ ,  $V_{20}(0)$ ,  $\psi_{210}(0)$  of the bound multiSFDM configuration. We solve it in a fixed range of  $(0, r_f)$  and we vary the boundary value  $N_T$  to find a family of solutions. In Fig. 1

<sup>6</sup>Notice that the mass scale of the configurations is

$$M_s = \frac{c^2}{G\tilde{\mu}} = 10^{12} M_\odot \left( \frac{10^{-22} \text{ eV}}{\mu c^2} \right)$$

and then the physical mass of the multistate configuration is obtained from  $\sqrt{\lambda} N M_s$ .

<sup>7</sup>This is the dimensionless variable  $v_h^2/c^2$  that has to be multiplied by  $\lambda$  once it is known, because of the scaling property  $v_h \rightarrow \sqrt{\lambda} v_h$ .

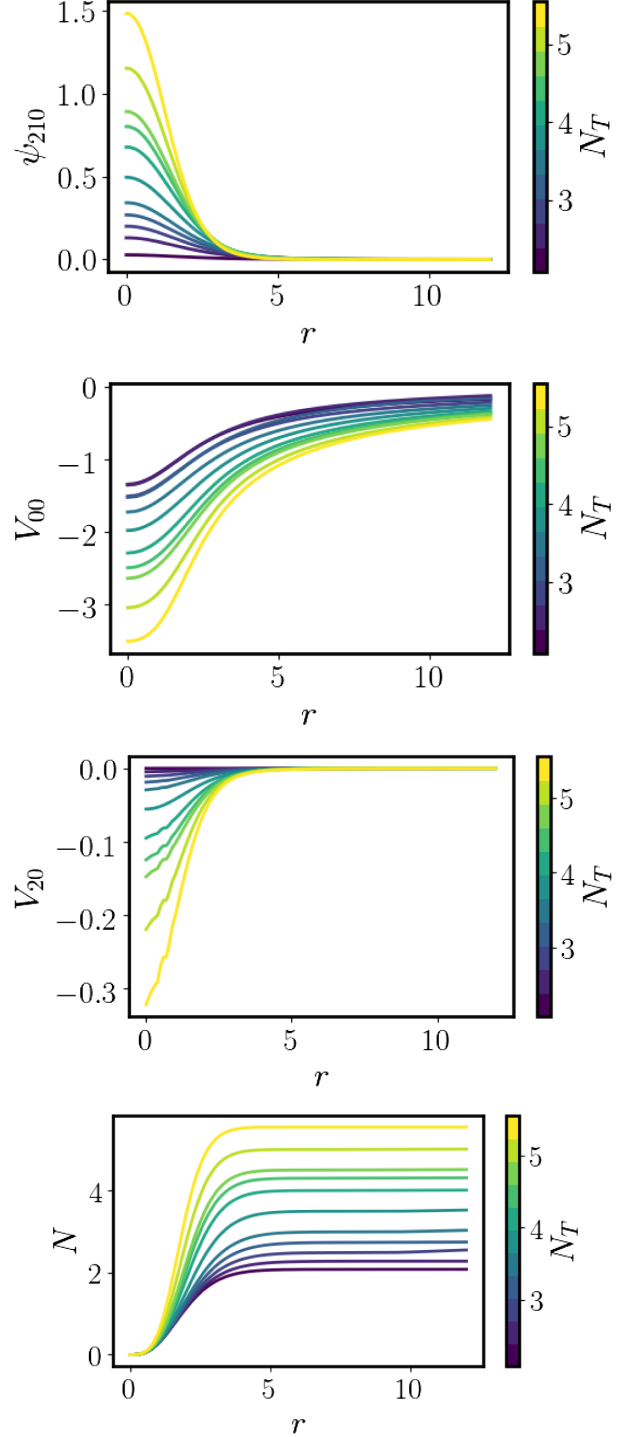


FIG. 1. Family of solutions of the multiSFDM ( $\Psi_{100}, \Psi_{210}$ ). The excited state radial function  $\psi_{210}$  (upper), first function  $V_{00}$  (middle panel) and second function  $V_{20}$  (next panel) in the expansion of the potential  $V$ , and the enclosed mass  $N(r)$  (bottom panel). In the color scale, the total mass  $N_T = N(r_f)$  of each of the solutions in the family is shown.

we show the plots of  $\psi_{210}$ ,  $V_{00}$ ,  $V_{20}$ , and the enclosed mass  $N$  for the family of solutions we found.

In Table I the different quantities that characterize each of the solutions of the family are shown: the total mass of

TABLE I. multiSFDM (100,210). Total mass of the configuration (column 1), energy eigenvalues of the ground (2) and excited state (3), total energy of the configuration (4), mass ratio between states of the configuration  $\eta = N_{210}(r_f)/N_{100}(r_f)$  (5), and amplitude ratio between states of the configuration  $\zeta = \psi_{100}(0)/\psi_{210}(0)$  (6).

$N_T$	$E_{100}$	$E_{210}$	$E_T$	$\eta$	$\zeta$
(1)	(2)	(3)	(4)	(5)	(6)
2.1	-0.69	-0.40	-0.69	0.01	37.27
2.3	-0.69	-0.40	-0.66	0.14	7.70
2.5	-0.84	-0.54	-0.77	0.29	5.01
2.7	-0.84	-0.54	-0.74	0.48	3.73
3.0	-1.03	-0.72	-0.90	0.71	2.93
3.5	-1.25	-0.92	-1.07	1.27	2.02
4.0	-1.51	-1.16	-1.28	1.97	1.47
4.3	-1.68	-1.31	-1.42	2.50	1.25
4.5	-1.80	-1.42	-1.52	2.90	1.12
5.0	-2.12	-1.71	-1.79	4.12	0.87
5.5	-2.49	-2.04	-2.11	5.83	0.67

the configuration  $N_T$  (that we use as the solution identifier within the family); the energy eigenvalues of the ground state  $E_{100}$  and the excited state  $E_{210}$ ; the total energy of the configuration  $E_T = (E_{100}N_{100} + E_{210}N_{210})/N_T$ ; the mass ratio  $\eta = N_{210}(r_f)/N_{100}(r_f)$  and amplitude ratio  $\zeta = \psi_{100}(0)/\psi_{210}(0)$  between states of the configuration.

In Fig. 2 we show as representative examples two cases of the dark matter mass density  $\rho = |\Phi_{100}|^2 + |\Phi_{210}|^2$  as a function of the  $(r, \theta)$  coordinates, one solution with  $N_T = 2.0$ , where the monopole term  $\psi_{100}$  dominates over

the dipole term  $\psi_{210}$ , and the solution with  $N_T = 5.5$  where the opposite happens.

### B. multiSFDM case (100, 200)

For the multiSFDM case  $(\Psi_{100}, \Psi_{200})$  the system (3) becomes

$$\nabla_{r_0}^2 \psi_{100}(r) = 2(V_{00} - E_{100})\psi_{100},$$

$$\nabla_{r_0}^2 \psi_{200}(r) = 2(V_{00} - E_{200})\psi_{200},$$

$$\nabla_{r_0}^2 V_{00}(r) = \psi_{100}^2 + \psi_{200}^2,$$

where the gravitational potential is simply

$$V(r, \theta) = \sqrt{4\pi}V_{00}(r)Y_{00}(\theta, \phi) = V_{00}(r)$$

and the circular velocity

$$v_h^2 = \frac{P_0}{r}. \quad (7)$$

In [47], these multistate configurations were shown to be stable only when  $N_{200}(r_f)/N_{100}(r_f) < 1.1$  so we restrict ourselves to work only with this kind of solutions. Once again we use the total mass  $N_T$  as a solution identifier within the family. In Table II we show the energy eigenvalues, the total energy, and the mass and amplitude ratios for each solution in the family. We also plot the corresponding family of solutions for this case in Fig. 3.

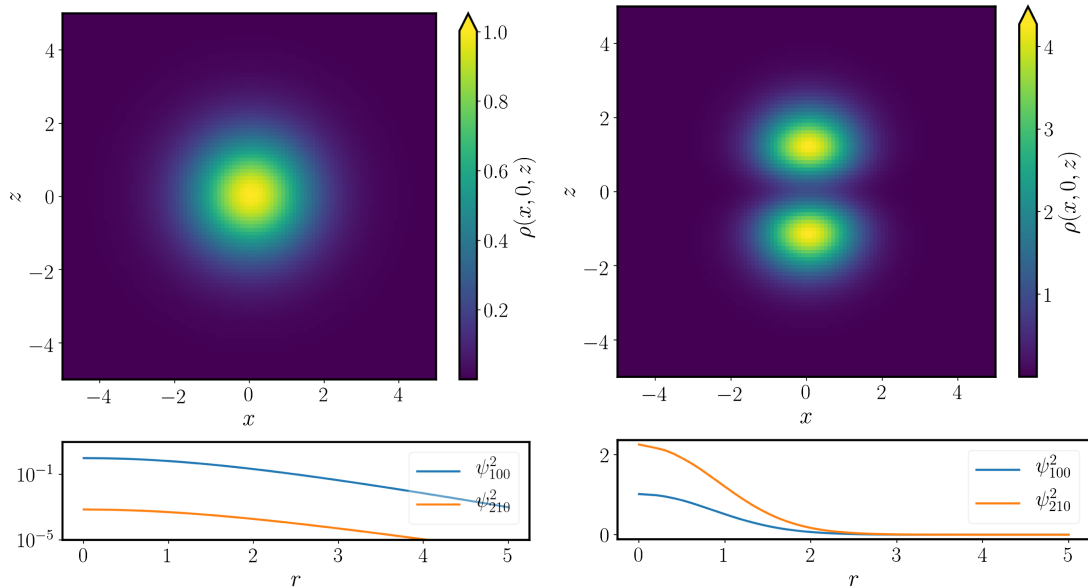


FIG. 2. Projection in the  $(x, z)$  plane of the dimensionless mass density as a function of the  $(x, y, z)$  dimensionless cartesian coordinates for the multiSFDM  $(\Psi_{100}, \Psi_{210})$ . The left panel shows the solution with  $N_T = 2.0$  where the monopole term  $\psi_{100}$  dominates over the dipole term  $\psi_{210}$ , and the right panel is the solution with  $N_T = 5.5$  where the excited state  $\psi_{210}$  dominates. In color scale, the mass density is shown.

TABLE II. Same as in Table I but now using state  $\psi_{200}$ .

$N_T$	$E_{100}$	$E_{200}$	$E_T$	$\eta$	$\zeta$
(1)	(2)	(3)	(4)	(5)	(6)
2.18	-0.737	-0.337	-0.71	0.07	6.00
2.30	-0.745	-0.341	-0.70	0.14	4.11
2.40	-0.766	-0.359	-0.70	0.20	3.37
2.50	-0.788	-0.377	-0.70	0.27	2.90
2.60	-0.811	-0.395	-0.71	0.34	2.56
2.66	-0.830	-0.412	-0.72	0.38	2.41
2.70	-0.834	-0.414	-0.71	0.41	2.31
2.75	-0.840	-0.418	-0.71	0.45	2.20
2.94	-0.917	-0.486	-0.76	0.59	1.89
2.97	-0.896	-0.463	-0.73	0.62	1.84
3.10	-0.925	-0.491	-0.75	0.71	1.75
3.30	-0.977	-0.532	-0.77	0.88	1.54
3.50	-1.032	-0.575	-0.80	1.07	1.37

### III. COADED ROTATION CURVES: DATA ANALYSIS

#### A. URCs theory

A coadded rotation curve is a representative rotation curve of a sample of galaxies with some particular properties in common (optical velocity  $v_{\text{opt}}$ , galaxy luminosity  $L_B$ , or absolute magnitude  $M_K$ ). Once the radial coordinate and circular velocity measurements are normalized, all these rotation curves have the same shape and can be represented by only one coadded rotation curve. In Fig. 4 we show the

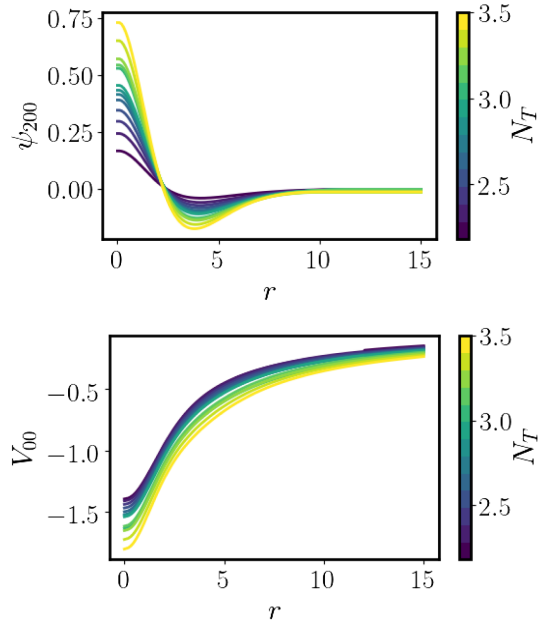


FIG. 3. Family of solutions of the multiSFDM ( $\Psi_{100}, \Psi_{200}$ ). The wave function  $\psi_{200}$  (upper panel) and the potential  $V$  (bottom panel). In the color scale, the total mass  $N_T$  of each of the solutions in the family is shown.

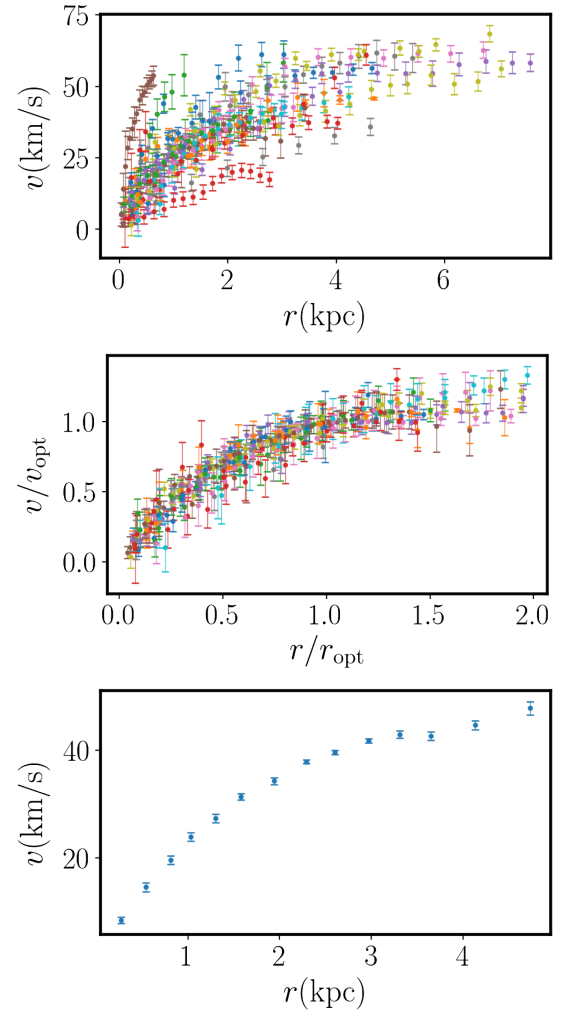


FIG. 4. Upper panel: Circular velocity measurements of 36 dwarf disc galaxies; middle panel: the normalized rotation curves; and bottom panel: the coadded rotation curves of dwarf disc galaxies. Data from [62].

circular velocity measurements, the normalized data, and the coadded rotation curve of the dwarf disc galaxies as an example.

The coadded rotation curve is constructed first by setting a unique binning in the radial coordinate to all individual normalized rotation curve. In each bin, there should be only one velocity measurement (if more, then the velocities are averaged). Once this procedure has been done for all individual rotation curves, the next step is to compile all individual rotation curves into only one coadded rotation curve, which is done by making a weighted average of all the velocity data in each bin.

The mass model of the coadded rotation curve is called URC. After finding the best-fitting parameters of the URC, we can apply the inverse transformation [described in [62]] to find the best-fitting parameters of each of the galaxies in the family.

## B. Mass models

### 1. Dwarf disc galaxies

We use the coadded rotation curve from [62] that comes from a sample of 36 dwarf disc galaxies from the local volume catalog [67]. These galaxies have an exponential disk scale length  $a_d$  in the range (0.18, 1.63) kpc and optical velocity  $v_{\text{opt}} = v(R_{\text{opt}})$  in the range (17, 61) km/s. The optical radius  $R_{\text{opt}} = 3.2a_d$ . Absolute magnitude  $M_K \in (-19.9, -14.2)$ .

To fit the coadded rotation curve of the dwarf spiral galaxies we use a simple model of a galaxy, consisting of a stellar disc, an HI disc, and a dark matter halo. The circular velocity of a particle due to these components is

$$v(r) = \sqrt{v_h^2 + v_d^2 + v_{\text{HI}}^2}$$

where  $v_h$ ,  $v_d$ , and  $v_{\text{HI}}$  are the circular velocities due to the halo and the stellar and HI discs, respectively.

The stellar disc is modeled using a razor-thin exponential disc profile whose surface mass density written in cylindrical coordinates  $(\rho, \phi, z)$  is given by

$$\Sigma_d(\rho) = \Sigma_0 e^{-\rho/a_d},$$

where  $a_d$  is the disc scale length, and  $\Sigma_0$  is the central surface density and it is related to the total mass of the disc  $M_d$  as  $M_d = 2\pi\Sigma_0 a_d^2$ . The circular velocity due to this density profile is [68]

$$v_d(r) = \sqrt{\frac{2GM_d y^2}{a_d} (I_0(y)K_0(y) - I_1(y)K_1(y))},$$

where  $I_n$  and  $K_n$  are the modified Bessel functions of the first and second kind, respectively, and we have defined  $y \equiv r/(2a_d)$ .

The HI disc is also modeled using a razor-thin exponential disc profile but with  $a_{\text{HI}} = 3a_d = 3R_{\text{opt}}/3.2$ ,  $R_{\text{opt}} = 2.5$  kpc and  $M_{\text{HI}} = 1.7 \times 10^8 M_\odot$ .

### 2. Low surface brightness galaxies

Reference [61] uses a sample of 72 LSB galaxies with optical velocities in the range  $v_{\text{opt}} \in (24, 300)$  km/s and classify it into five groups (bins) depending on its optical velocity. Bin 1 with 13 galaxies,  $v_{\text{opt}} \in (24, 60)$  km/s and mean disc scale length  $a_d = 1.7$  kpc. Bin 2 with 17 galaxies,  $v_{\text{opt}} \in (60, 85)$  km/s and mean disc scale length  $a_d = 2.2$  kpc. Bin 3 with 17 galaxies,  $v_{\text{opt}} \in (85, 120)$  km/s and mean disc scale length  $a_d = 3.7$  kpc. Bin 4 with 15 galaxies,  $v_{\text{opt}} \in (120, 154)$  km/s and mean disc scale length  $a_d = 4.5$  kpc. Bin 5 with 10 galaxies,  $v_{\text{opt}} \in (154, 300)$  km/s and mean disc scale length  $a_d = 7.9$  kpc. When the individual rotation curve of the galaxies within a group are expressed in

a normalized radius  $r/R_{\text{opt}}$  they all have almost the same distribution of matter. For each bin, [61] calculated the coadded rotation curve (see Fig. 5).

We model LSB galaxies with a stellar disc and a dark matter halo. To streamline the data Markov Chain Monte Carlo (MCMC) fitting process, as a first approximation, we neglected the contribution of an HI gaseous disc. In fact, [61] showed that this assumption does not affect the mass modeling. The circular velocity of a particle due to these components is

$$v(r) = \sqrt{v_h^2 + v_d^2}$$

where  $v_h$  and  $v_d$  are the circular velocities due to the halo and the stellar disc, respectively. The stellar disc is modeled with the same exponential profile as the dwarf disc galaxies. For each coadded rotation curve we use the mean disc scale length, so we end up with only one disc parameter  $M_d$ .

In the case of bin 5, we also consider a galaxy bulge that is modeled using a velocity profile as suggested in [61]:

$$v_b(r) = v_{\text{in}} \sqrt{\alpha \frac{r_{\text{in}}}{r}},$$

where  $r_{\text{in}} = 0.2a_d$  is the radius of the innermost measure of the rotation curve circular velocity  $v_{\text{in}} = 127$  km/s, thus the only bulge parameter to fit is the  $\alpha$  parameter.

For the dark matter component we will use the circular velocity profiles [Eqs. (6) and (7)] of all multistate configurations we have presented (see Fig. 6). Strictly speaking, our analysis should not be limited solely to the family of states that we have presented. However, exploring the entire parameter space of our system would result in a very large computational effort. For this reason, by restricting ourselves to this family of states, which cover different mass scales of the configurations quite well, we believe that it will be sufficient to give an estimate of the mass

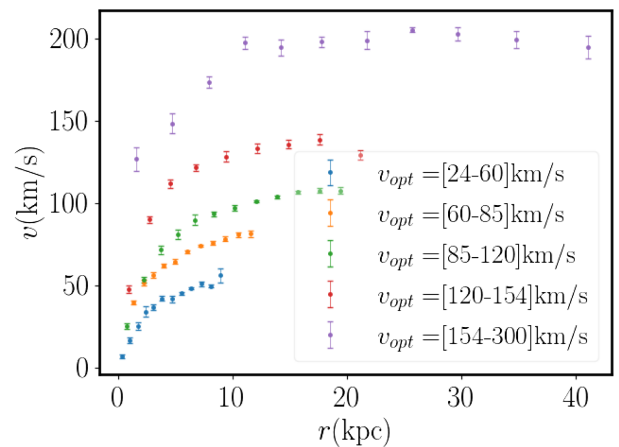


FIG. 5. Coadded rotation curves for each of the five bins of the low surface brightness galaxies. Data from [61].



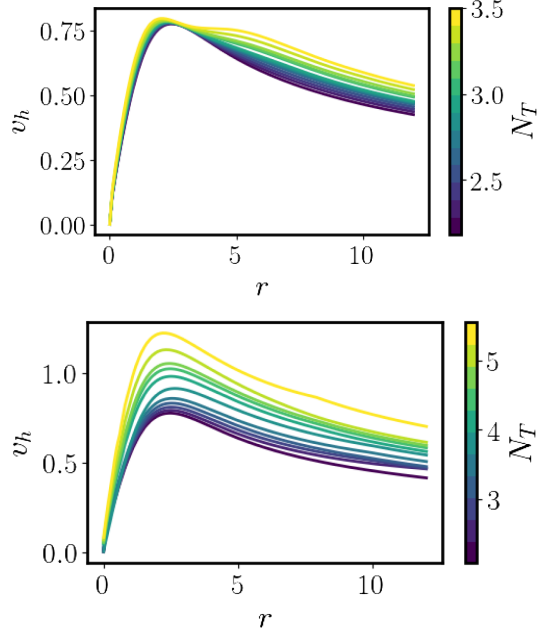


FIG. 6. Circular velocity  $v_h$  for the  $(\Psi_{100}, \Psi_{200})$  family (upper panel), the  $(\Psi_{100}, \Psi_{210})$  family (bottom panel). In the color scale, the total mass  $N_T$  of each of the solutions in the family is shown.

parameter of our model. In addition, with our results, we can also put this model into context with the CDM model, which we will do later.

Summarizing, we have a total of three parameters to fit, namely,  $\sqrt{\lambda}$  [remember the scaling property described in Eq. (4)],  $\tilde{\mu}$ , and  $M_d$ , except for the case of bin 5 where we have an extra fitting parameter  $\alpha$ . When only a single state is considered there are two free parameters for our model, the particle effective mass  $\tilde{\mu}$  and the scaling parameter  $\lambda$ , but whenever more states are considered, extra free parameters appear, for example, the ratio between total masses  $\eta$ . Because of the complexity of finding solutions, it is not possible to take  $\eta$  as a continuous parameter, so we will use a set of fixed solutions within each family and discriminate between them.

### C. Statistical calibration method

We use the MCMC method sampling the parameter space from uniform priors (see Table III). For a better

understanding of this method, we recommend reviewing [69].

For each of the configurations of multiSFDM, we use  $5 \times 10^4$  steps with 30% burn-in and 50 walkers to sample the parameter space. The results for each one of the varied parameters were calculated using the Lmfit [70] and Emcee [71] Python packages.

## IV. RESULTS AND DISCUSSION

### A. Dwarf disc galaxies

We performed the fit of the dwarf disc galaxies coadded rotation curve with each of the solutions of both multiSFDM families. We select the best fit in each family using the Akaike information criterion (AIC) and the Bayesian information criterion (BIC). AIC gives a measure of the fit of a given model to the data. It measures the goodness of a fit and it gives a penalty on the number of parameters in the model. If the model is simpler (has few parameters) the penalty is less. The lower AIC value says that the model has better performance. The BIC works as the AIC but with a different penalty in the number of parameters in the model. In AIC, the penalty is  $2k$ , with  $k$  being the number of parameters of the model, and in BIC the penalty is  $\ln(n)k$ ,  $n$  being the number of data points to fit.

To see whether the multistates give a better fit of the rotation curves, we also made the adjustment considering the dark matter halo in the ground state  $\Psi_{100}$ , which is commonly used to describe the core in SFDM galaxies and it is also typically used to model dwarf-sized galaxies. To do that, we use the Gaussian ansatz [37,41,72]:

$$\rho(r) = \frac{M}{(\pi R_c^2)^{3/2}} e^{-r^2/R_c^2} \quad (8)$$

as an approximation of the ground state density. We decided to use this Gaussian profile since previous works see, for example, [41] have shown that this profile can very well describe the numerical solution of the ground state configuration of the Schrödinger-Poisson system. In Table IV we present the results of the fits.

If we use the AIC, BIC, and  $\chi_{\text{red}}^2$  we can state that the best fit is obtained with the multiSFDM  $(\Psi_{100}, \Psi_{210})$

TABLE III. Uniform priors used in the MCMC fitting.

Parameter	Dwarf disc	LSB				
		bin 1	bin 2	bin 3	bin 4	bin 5
(1)	(2)	(3)	(4)	(5)	(6)	(7)
$\sqrt{\lambda}$	$[10^{-7}, 1]$	$[10^{-7}, 1]$	$[10^{-7}, 1]$	$[10^{-7}, 1]$	$[10^{-7}, 1]$	$[10^{-7}, 1]$
$\mu$ (eV/ $c^2$ )	$[10^{-26}, 10^{-18}]$	$[10^{-26}, 10^{-18}]$	$[10^{-26}, 10^{-18}]$	$[10^{-26}, 10^{-18}]$	$[10^{-26}, 10^{-18}]$	$[10^{-27}, 10^{-19}]$
$M_d(10^{10}M_\odot)$	$[10^{-6}, 10^0]$	$[10^{-5}, 10^1]$	$[10^{-6}, 10^1]$	$[10^{-6}, 10^1]$	$[10^{-5}, 10^2]$	$[10^{-5}, 10^2]$
$\alpha$						$[10^{-6}, 10]$

TABLE IV. Fit results for the dwarf disc galaxies coadded rotation curve. MultiSFDM family name (column 1), the total mass of the configuration (2), reduced  $\chi^2$  (3), the Akaike information criterion (4), the Bayesian information criterion (5), SFDM particle mass (6), scaling parameter (7), stellar disc mass (8), and total halo mass  $M_T$  (9).

Family	$N_T$	$\chi^2_{\text{red}}$	AIC	BIC	$\mu \pm \sigma_\mu$ ( $10^{-24}$ eV/ $c^2$ )	$\sqrt{\lambda} \pm \sigma_{\sqrt{\lambda}}$ ( $\times 10^{-3}$ )	$M_d \pm \sigma_{M_d}$ ( $10^7 M_\odot$ )	$M_T$ ( $10^{10} M_\odot$ )
(1)	(2)	(3)	(4)	(5)	(6)	(7)	(8)	(9)
$\Psi_{100}$	1.5	1.6	9.5	11.4	$17.4 \pm 0.6$	$0.191 \pm 0.001$	$12.00 \pm 1.37$	0.225
$(\Psi_{100}, \Psi_{200})$	2.6	1.50	8.29	10.2	$18.3 \pm 1.0$	$0.183 \pm 0.002$	$4.34 \pm 1.76$	0.347
$(\Psi_{100}, \Psi_{210})$	3.5	1.27	6.01	7.9	$23.8 \pm 1.2$	$0.154 \pm 0.002$	$10.28 \pm 1.49$	0.301

NOTE—We only show the result of the best fit per family.

configuration, particularly the solution characterized with the total mass  $N_T = 3.5$  (physical mass  $M_T = \sqrt{\lambda} M_s N_T = 3.01 \times 10^9 M_\odot$ ) and having a particle effective mass  $\mu = (2.38 \pm 0.12) \times 10^{-23}$  eV/ $c^2$ . In the upper panel of Fig. 7 we show the plot of the fit and the contribution of the disc, HI disc, and dark matter separately; and in the bottom panel we show a corner plot of the posterior distribution of the fitting parameters. In Table VIII of the Appendix the

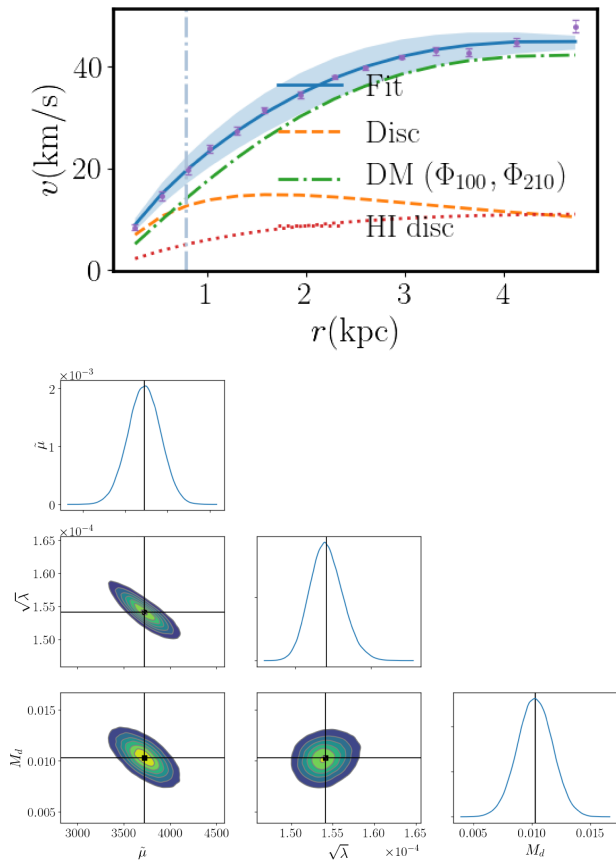


FIG. 7. Upper panel: Dwarf Disc galaxies coadded rotation curve. The disc, HI disc, and dark matter contributions are also shown. Dark matter is in the multiSFDM  $(\Psi_{100}, \Psi_{210})$ . The best-fit parameters are shown in Table IV. The horizontal line is the disc characteristic length  $a_d$ . Bottom panel: We show the posterior distribution of parameters, as an example, in this case. Particle mass  $\tilde{\mu}$  is in 1/kpc units and disc mass  $M_d$  is in  $10^{10} M_\odot$  units.

parameters of each of the dwarf disc galaxies used to form the coadded rotation curve are given.

The fit with this dark matter model is consistent with having a stellar disc mass  $M_d \approx 10^8 M_\odot$ , which is also consistent with the one obtained in [62] with the Burkert profile as dark matter model.

## B. LSB galaxies

As in the case of the dwarf disc galaxies, we also perform the fit of the five different bins of the LSB galaxies coadded rotation curve with each of the solutions of both multiSFDM families. We select the best fit in each family using the AIC and BIC parameters and in Table V we present the results of the best fit found for each of the two families of configurations for all five bins. For bins 1, 2, and 3 we also show the best fit using only the ground state as the dark matter halo with the Gaussian ansatz. For bins 4 and 5, it is not possible to fit the coadded rotation curve using a single state since the rotation curve of the ground state falls too fast to explain the flatness of the observed rotation curve at large radii. This is expected since these bins are where the largest and most massive galaxies belong, so it would be expected that the ground state alone would not be able to model these galaxies.

For the LSB bin 1 (see also Fig. 8) the best fit between families was achieved with the  $(\Psi_{100}, \Psi_{210})$  configuration, specifically the solution labeled by  $N_T = 3.5$  (physical mass  $M_T = 7.7 \times 10^9 M_\odot$ ) and a particle effective mass  $\mu = (1.05 \pm 0.14) \times 10^{-23}$  eV/ $c^2$ . In Table IX of the Appendix the parameters of each of the LSB bin 1 galaxies used to form the coadded rotation curve are given.

For the largest LSB galaxies, the particle effective mass is smaller  $\mu = O(10^{-24}) - O(10^{-25})$  eV/ $c^2$ , the same order of magnitude that spiral galaxies like the Milky Way have [73]. However, it would be expected that the reason why these lighter masses are preferred in these bins is because the largest and most massive galaxies belong to it, so configurations with only one excited state should not describe this type of galaxies correctly and then, the smaller mass is introduced to account for the missing multistate configurations.

For bin 5, let us consider for example, a three-state spherically symmetric multistate configuration made of the

TABLE V. Fit results for the LSB galaxies coadded rotation curves. LSB bin number (column 1), multiSFDM family name (2), total mass of the configuration (3), reduced  $\chi^2$  (4), the Akaike information criterion (5), the Bayesian information criterion (6), SFDM particle mass (7), scaling parameter (8), stellar disc mass (9), bulge parameter (10), and total halo mass in physical units  $M_T$  (11).

Bin	Family	$N_T$	$\chi^2_{\text{red}}$	AIC	BIC	$\mu \pm \sigma_\mu$ ( $10^{-24}$ eV/ $c^2$ )	$\sqrt{\lambda} \pm \sigma_{\sqrt{\lambda}}$ ( $\times 10^{-3}$ )	$M_d \pm \sigma_{M_d}$ ( $10^7 M_\odot$ )	$\alpha \pm \sigma_\alpha$	$M_T$ ( $10^{10} M_\odot$ )
(1)	(2)	(3)	(4)	(5)	(6)	(7)	(8)	(9)	(10)	(11)
1	$\Psi_{100}$	1.5	1.3	6.1	7.6	$7.3 \pm 0.7$	$0.214 \pm 0.003$	$63.5 \pm 11.9$		0.60
	$(\Psi_{100}, \Psi_{200})$	3.10	1.44	6.900	8.3	$7.4 \pm 1.02$	$0.205 \pm 0.005$	$37.5 \pm 16.0$		1.14
	$(\Psi_{100}, \Psi_{210})$	3.5	1.29	5.624	7.1	$10.5 \pm 1.40$	$0.173 \pm 0.005$	$55.0 \pm 13.5$		0.77
2	$\Psi_{100}$	1.3	1.2	4.1	5.3	$2.1 \pm 0.4$	$0.374 \pm 0.021$	$411.7 \pm 19.9$		3.09
	$(\Psi_{100}, \Psi_{200})$	2.94	1.02	2.677	3.9	$2.0 \pm 0.47$	$0.350 \pm 0.030$	$362.5 \pm 20.0$		6.72
	$(\Psi_{100}, \Psi_{210})$	5.5	0.91	1.496	2.7	$3.4 \pm 0.55$	$0.221 \pm 0.014$	$354.9 \pm 19.3$		4.81
3	$\Psi_{100}$	0.8	0.2	-17.4	-16.0	$1.20 \pm 0.13$	$0.446 \pm 0.022$	$1381.5 \pm 66.4$		3.94
	$(\Psi_{100}, \Psi_{200})$	3.50	0.19	-17.211	-15.8	$1.1 \pm 0.16$	$0.419 \pm 0.020$	$1238.0 \pm 70.8$		18.24
	$(\Psi_{100}, \Psi_{210})$	3.5	0.19	-17.299	-15.8	$1.6 \pm 0.23$	$0.361 \pm 0.017$	$1349.8 \pm 66.6$		10.47
4	$(\Psi_{100}, \Psi_{200})$	2.18	5.24	17.255	17.8	$1.3 \pm 0.26$	$0.373 \pm 0.027$	$4295.4 \pm 131.0$		8.33
	$(\Psi_{100}, \Psi_{210})$	5.5	4.77	16.410	17.0	$1.4 \pm 0.40$	$0.262 \pm 0.026$	$4280.4 \pm 128.9$		13.71
5	$(\Psi_{100}, \Psi_{200})$	2.50	1.73	9.086	10.7	$0.24 \pm 0.16$	$0.716 \pm 0.196$	$16806.5 \pm 576.9$	$0.8 \pm 0.1$	97.89
	$(\Psi_{100}, \Psi_{210})$	4.0	1.73	9.076	10.7	$0.39 \pm 0.21$	$0.525 \pm 0.117$	$16793.1 \pm 583.1$	$0.8 \pm 0.1$	71.11

NOTE—We only show the result of the best fit per family.

first three spherical states ( $\Psi_{100}, \Psi_{200}, \Psi_{300}$ ), with energy eigenvalues  $E_{100} = -1.35$ ,  $E_{200} = -0.82$ , and  $E_{300} = -0.54$ , the configuration have a total mass  $N_T = 4.51$ . In Fig. 9 we show the plot of the solution, the three wave functions  $\psi_{100}$  (zero nodes),  $\psi_{200}$  (one node),  $\psi_{300}$  (two nodes), and the potential  $V$ .

In Fig. 10 we show the fit of the LSB bin 5 coadded rotation curve, the effective mass of the multiSFDM  $\mu = (1.24 \pm 0.06) \times 10^{-24}$  eV/ $c^2$  becomes bigger than for a two-state configuration. The rest of the fit parameters take the values  $\sqrt{\lambda} = (0.777 \pm 0.009) \times 10^{-3}$ ,  $M_d = (646.8 \pm 315.3) \times 10^7 M_\odot$ , and  $\alpha = 0.8 \pm 0.1$ . We note that this configuration, besides that it allows a bigger dark matter particle mass, has the ripples seen in the data.

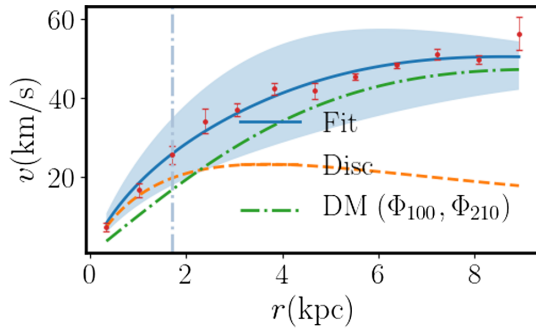


FIG. 8. LSB bin 1 galaxies coadded rotation curve. The disc and dark matter contributions are also shown. Dark matter is in the multiSFDM ( $\Psi_{100}, \Psi_{210}$ ). The best-fit parameters are shown in Table V. The horizontal line is the disc characteristic length  $a_d$ .

This confirms that in the most massive galaxies, the higher energy excited states have a greater effect on modeling the galaxy. It is clear then that our two-state configurations scenario should be applied only for the less massive galaxies and that the addition of more excited states increases the particle mass to agree with the order of magnitude found in dwarf galaxies.

In Fig. 11 the baryonic fraction  $M_d/M_h$  as a function of the halo mass  $M_d$  is plotted for all LSB bins and dwarf disc galaxies. The empirical relation of [74] is also shown as a comparison with the CDM results.

In cored profiles an interesting quantity to calculate is the central surface density. For doing that we first define the dark matter characteristic radius  $r_c$  as the radius at which the density of the ground state component of the

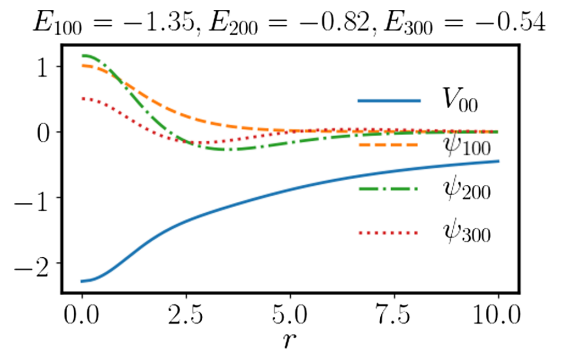


FIG. 9. Three-state ( $\Psi_{100}, \Psi_{200}, \Psi_{300}$ ) multistate configuration. The three wave functions and the gravitational potential are shown.

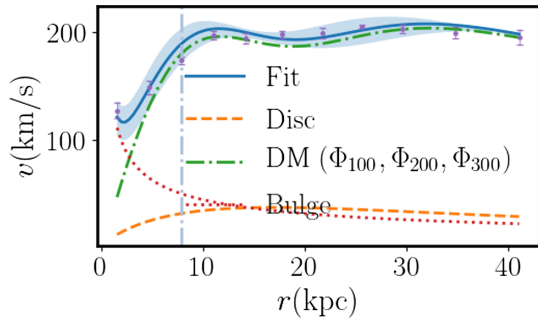


FIG. 10. LSB bin 5 fit with a three-state ( $\Psi_{100}, \Psi_{200}, \Psi_{300}$ ) spherically symmetric multistate configuration. The scalar dark matter mass  $\mu = (1.24 \pm 0.06) \times 10^{-24}$  eV/ $c^2$  becomes bigger than for a two-states configuration.

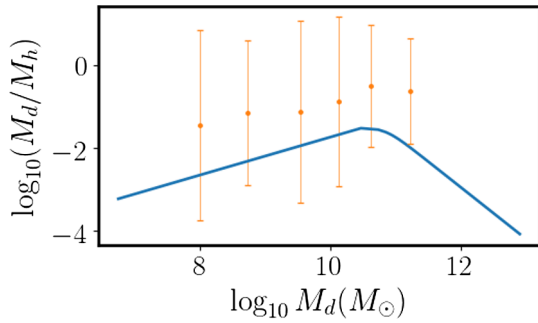


FIG. 11. The baryonic fraction  $M_d/M_h$  as a function of the halo mass  $M_d$  for dwarf disc and LSB bins 1 to 5. The blue line is the relation of [74].

multiSFDM configuration  $\rho_{100}(r) \equiv |\Psi_{100}(r)|^2$  drops to the half of its initial value:

$$\rho_{100}(r_s) = 0.5\rho_{100}(0).$$

The dark matter central surface density is then defined as

$$\Sigma_0 = \rho_0 r_c \quad (9)$$

where  $\rho_0$  is the dark matter density at  $r = 0$ .

In Fig. 12 the dark matter central surface density  $\Sigma_0$  is plotted for all bins and each galaxy. As in the case of other cored profiles, the central surface density is almost constant and independent of the baryonic characteristics as luminosity or absolute magnitude [75]. For the multiSFDM model, the central surface density has a value of  $\log_{10}(\Sigma_0/M_\odot \text{pc}^{-2}) = 1.24 \pm 0.07$ .

It is worth mentioning that in [76] (see also [40]) it was shown that the constancy of this central surface density is a direct consequence of assuming the radial acceleration relation (RAR) to be valid, with the latter being an empirical function between the observed acceleration in stars and the acceleration inferred to be produced by baryons. That is, in the case of assuming a dark matter profile that possesses a core (as is the case in our scenario),

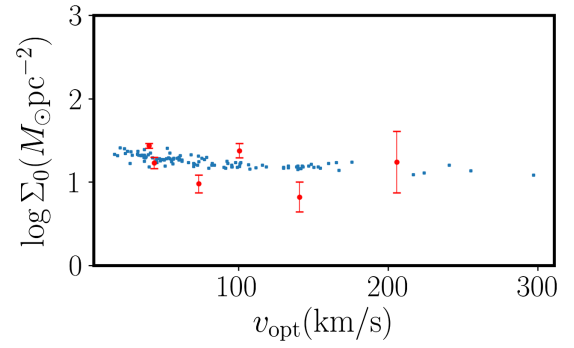


FIG. 12. Dark matter central surface density  $\Sigma_0 = \rho_0 r_c$  as a function of the optical velocity  $v_{\text{opt}}$ . Red markers are the quantities calculated from the dwarf disc and LSB bins, and blue markers are calculated for the individual galaxies belonging to each bin.

this RAR predicts that the central cores in all galaxies must comply with  $\Sigma_0 = Cte$ , thus making this a universal constant for all galaxies.

### C. NFW

From  $N$ -body simulations of CDM, [8] found an equilibrium density profile for dark matter halos

$$\rho(r) = \frac{\rho_0}{(r/r_s)(1+r/r_s)^2}$$

where  $r_s$  is the scale radius and  $\rho_0$  is a characteristic density.

The halo circular velocity contribution is

$$v_h = \sqrt{\frac{GM(r)}{r}}, \quad (10)$$

where  $M(r)$  is the enclosed mass at radius  $r$  given by

$$M(r) = 4\pi r_s^3 \rho_0 \left( -\frac{r}{r+r_s} + \ln\left(\frac{r+r_s}{r}\right) \right), \quad (11)$$

which give us a two-parameter  $(r_s, \rho_0)$  profile.

We performed the same MCMC fitting procedure we did with the SFDM model. In Table VI we show the results for the LSB bins 1 to 5, the reduced  $\chi^2$ , the AIC and BIC criteria, and the best-fitting parameters. For the case of dwarf disc galaxies, we could not fit the rotation curves with the NFW profile, which is consistent with the fact that dwarf disc galaxies necessarily need a core to be able to explain their rotation curves.

Comparing the AIC, BIC, and  $\chi^2$  we see that multiSFDM can better describe the LSB coadded rotation curve for bins 1, 2, 3, and 5 than the NFW profile. This turns out to be very interesting, since our model, as simple as it seems in only adopting two-state configurations, seems to fit the data better than the standard cosmological model. It is clear that if we continue to increase the number of states, we will

TABLE VI. LSB rotation curves fitting results with an NFW profile. Velocity bin (column 1), reduced  $\chi^2$  (2), the Akaike information criterion (3), the Bayesian information criterion (4), stellar disc mass (5), scale radius (6), and characteristic density (7).

Bin	$\chi^2_{\text{red}}$	AIC	BIC	$M_d \pm \sigma_{M_d}$ ( $10^7 M_\odot$ )	$r_s \pm \sigma_{r_s}$ (kpc)	$\rho_0 \pm \sigma_{\rho_0}$ ( $10^{-4} M_\odot/\text{pc}^3$ )
(1)	(2)	(3)	(4)	(5)	(6)	(7)
1	4.23	19.84	21.3	$19.2 \pm 10.88$	$64.4 \pm 23.1$	$2.156 \pm 1.076$
2	1.72	4.91	6.4	$168.5 \pm 47.91$	$34.8 \pm 23.1$	$8.235 \pm 5.979$
3	1.14	4.16	5.6	$873.7 \pm 73.70$	$109.1 \pm 43.4$	$2.162 \pm 1.004$
4	1.51	6.06	6.7	$2144.1 \pm 465.47$	$14.2 \pm 2.7$	$52.398 \pm 20.356$
5	1.78	9.39	11.0	$12891.1 \pm 1229.26$	$47.6 \pm 20.6$	$9.275 \pm 6.097$

TABLE VII. LSB rotation curves fitting results with a diCintio profile. Velocity bin (column 1), reduced  $\chi^2$  (2), the Akaike information criterion (3), the Bayesian information criterion (4).

Bin	$\chi^2_{\text{red}}$	AIC	BIC	$M_d \pm \sigma_{M_d}$ ( $10^7 M_\odot$ )	$r_s \pm \sigma_{r_s}$ (kpc)	$M_h \pm \sigma_{M_h}$ ( $10^7 M_\odot$ )
(1)	(2)	(3)	(4)	(5)	(6)	(7)
1	1.01	2.63	4.1	$18.9 \pm 16.20$	$4.174 \pm 1.283$	$2923.591 \pm 709.820$
2	0.87	0.95	2.1	$1.4 \pm 0.34$	$48.537 \pm 29.750$	$30135.090 \pm 11948.730$
3	0.91	1.37	2.8	$3.9 \pm 0.64$	$8.660 \pm 1.289$	$21268.698 \pm 1590.216$

adjust the rotation curves better and better, which will reduce the  $\chi^2$  of our model, although this will also result in a greater penalty for the model. In this way, we would expect there to be a preferred number of states where the value of our selection criteria (AIC and BIC) would be reduced to the minimum, even less than those reported by our model with only two states. Thus, we would expect that, in general, the multiSFDM model would be preferred for universal rotation curves to CDM.

#### D. diCintio profile

As the NFW profile is based in CDM-only simulations, [77] introduced a double power-law dark matter density profile to account for stellar feedback

$$\rho = \frac{\rho_0}{\left(\frac{r}{r_s}\right)^\gamma \left(1 + \left(\frac{r}{r_s}\right)^\alpha\right)^{(\beta-\gamma)/\alpha}} \quad (12)$$

where  $\alpha$ ,  $\beta$ , and  $\gamma$  are found by fitting the profile to hydrodynamical simulations. [77] found the best fit of the parameters as a function of the stellar-to-halo mass ratio  $M_d/M_h$ , giving

$$\alpha = 2.94 - \log_{10}((10^{X+2.33})^{-1.08} + (10^{X+2.33})^{2.29})$$

$$\beta = 4.23 + 1.34X + 0.26X^2$$

$$\gamma = -0.06 + \log_{10}((10^{X+2.56})^{-0.68} + 10^{X+2.56})$$

where  $X = \log_{10}(M_d/M_h)$ . The NFW profile is recovered when  $(\alpha, \beta, \gamma) = (1, 3, 1)$ . The free parameters to fit the rotation curves are then the scale radius  $r_s$ , the stellar mass  $M_d$ , and the halo mass  $M_h$ .

In Table VII we show the results for the LSB bins 1 to 3, the reduced  $\chi^2$ , the AIC and BIC criteria, and the best fitting parameters. Bin 4 and 5 should be still modeled with the NFW profile since the diCintio profile for large halo masses becomes the NFW profile.

All three bins have better fits with the diCintio profile than with the multistate SFDM model, but with a much smaller stellar-mass  $M_d = O(10^7)M_\odot$ , they have been inconsistent with the results of [61] using a cored Burkert profile.

#### V. CONCLUSIONS

In this work we consider spherically symmetric and axisymmetric multistate scalar dark matter as dark matter halos in dwarf disc and low surface brightness galaxies. The multistate configurations are equilibrium solutions of the Gross-Pitaevskii-Poisson equations when the boson particles are in more than one state. Particularly, we work in multistate configurations where bosonic particles are able to be in the ground state ( $\Psi_{100}$ ) and one excited state ( $\Psi_{210}$  or  $\Psi_{200}$ ).

We test this model by fitting coadded rotation curves of LSB galaxies and dwarf disc galaxies using an MCMC method. We determine the parameters that provide the best fit to data. The resulting parameters of the baryonic mass model are consistent with the ones found in similar works that use different dark matter models [61,62].

Both in LSB galaxies and in dwarf disc galaxies do the multistates models fit better the rotation curves than a single ground state. In LSB bins 1, 2, 3, and 5 the multistate models fit better the rotation curves than the NFW profile; only in LSB bin 4 galaxies NFW profile describes better the

rotation curve. The diCintio profile, a CDM profile that accounts for stellar feedback, shows better fits than the multiSFDM model with the disadvantage that they require a really low stellar mass  $M_d$ . It should be mentioned that, in order for the multiSFDM model to be correctly compared with the phenomenological model of diCintio, it would also be necessary to consider the effect of stellar feedback in multiSFDM, which we have not considered in this work.

For the dwarf disc galaxies we obtained a better fit with the  $(\Psi_{100}, \Psi_{210})$  configuration than with the  $(\Psi_{100}, \Psi_{200})$  and the ground state alone  $\Psi_{100}$  configurations, obtaining a SFDM particle effective mass  $\mu = 2.38 \pm 0.12 \times 10^{-23} \text{ eV}/c^2$ . Similarly for the LSB bin 1 a particle effective mass  $\mu = 1.05 \pm 0.14 \times 10^{-23} \text{ eV}/c^2$  is obtained for the better fit with the  $(\Psi_{100}, \Psi_{210})$  configuration. In the most massive LSB galaxies (bins 2 to 5) the particle effective mass is smaller  $\mu = O(10^{-24}) - O(10^{-25}) \text{ eV}/c^2$ . This last result is expected since smaller masses of the SFDM particle allow for more extended configurations in the scenarios studied here, which in turn enables a less pronounced Keplerian fall for small radii. Of course, this smaller mass parameter for large galaxies is only a consequence of not introducing a complete family of multistate configurations, as we explained in the Introduction, however, the computational difficulty of building configurations of many multistates does not allow us to freely test them.

The addition of excited states postpones the Newtonian drop in the circular velocity to greater distances, which makes it have a smaller extension and therefore a greater particle mass.

These results encourage further studies on different configurations of multistate scalar field dark matter halos with a greater number of states that could fit better the larger galaxies and have consistent bounds of the scalar field particle mass.

*Software:* Lmfit Python package [70], Emcee Python package [71].

### ACKNOWLEDGMENTS

This work was partially supported by CONACyT México under Grants No. A1-S-8742, 304001, 376127; Project No. 269652 and Fronteras Project 281; I0101/131/07

C-234/07 of the Instituto Avanzado de Cosmología (IAC) collaboration [78]. The authors are grateful for the computing time granted by LANCAD and CONACyT in the Supercomputer Hybrid Cluster “Xihcoatl” at GENERAL COORDINATION OF INFORMATION AND COMMUNICATIONS TECHNOLOGIES (CGSTIC) of CINVESTAV. URL: [79] and Abacus clusters at Cinvestav, IPN. J. S. acknowledges financial support from a CONACyT doctoral fellowship. L. P. acknowledges sponsorship from CONACyT through Grant No. CB-2016-282569.

### APPENDIX: DENORMALIZATION PROCESS

The denormalization process allows us to find the parameters of the mass model for each of the galaxy members in the coadded rotation curves. For doing that we first note that the scale radius  $r_c$  and disc scale length  $a_d$  of the dwarf disc and all the LSB bins are correlated (see Fig. 13), the correlation can be fitted yielding to

$$\log_{10} r_c = 0.41 + 1.33 \log_{10} a_d. \quad (\text{A1})$$

This expression can give us the core radius of any of the members of the LSB or dwarf disc galaxies in the coadded rotation curves as a function of its measured disc scale length.

Similarly there is a correlation between the disc scale length and the dark matter central density  $\rho_0$  and the virial radius  $r_{\text{vir}}$  (see Fig. 13). The logarithmic fit results in

$$\log_{10} \rho_0 = -3.13 - 1.49 \log_{10} a_d, \quad (\text{A2})$$

and

$$\log_{10} r_{\text{vir}} = 1.15 + 1.28 \log_{10} a_d. \quad (\text{A3})$$

This last expression allows us to know the virial radius of each individual galaxy and hence the halo virial mass  $M_{\text{vir}} = M_h(r_{\text{vir}})$ .

As mentioned in [61,62] the good fit and the small intrinsic scatter of the coadded rotation curve allow us to write

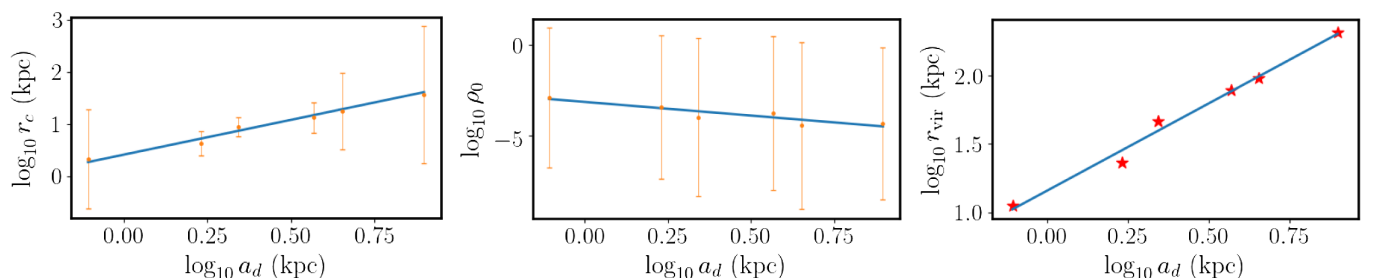


FIG. 13. Core radius, dark matter central density, and virial radius as a function of the disc scale length of the dwarf disc and all LSB bins. The blue line is the logarithmic fit.

$$\frac{M_{d,i}}{v_{\text{opt},i}^2 R_{\text{opt},i}} = \frac{M_d}{v_{\text{opt}}^2 R_{\text{opt}}} = \text{cte} \quad (\text{A4})$$

and

$$\frac{M_{\text{HI},i}}{v_{\text{opt},i}^2 R_{\text{opt},i}} = \frac{M_{\text{HI}}}{v_{\text{opt}}^2 R_{\text{opt}}} = \text{cte} \quad (\text{A5})$$

where  $M_{d,i}$ ,  $M_{\text{HI},i}$ ,  $v_{\text{opt},i}$ ,  $R_{\text{opt},i}$  are, respectively, the disc mass, HI disc mass, optical velocity, and optical radius of the individual galaxies conforming the coadded rotation curve. The quantities without the  $i$  index are the mean quantities of the coadded rotation curve that we had been working with. As  $v_{\text{opt},i} R_{\text{opt},i}$  are known quantities for each galaxy using Eqs. (A4) and (A5) it is possible to find the disk mass  $M_{d,i}$ ,  $M_{\text{HI},i}$  of each galaxy.

In Tables VIII and IX the parameters of all the dwarf disc galaxies and LSB bin 1 galaxies are shown.

TABLE VIII. Mass model parameters of the dwarf disc galaxies.

Name	$a_d$ kpc	$v_{\text{opt}}$ km/s	$r_c$ kpc	$M_d$ $10^7 M_{\odot}$	$M_h(R_{\text{opt}})$ $10^{10} M_{\odot}$	$M_{\text{vir}}$ $10^{10} M_{\odot}$	$M_{\text{HI}}$ $10^7 M_{\odot}$	$M/L$ $M_{\odot}/L_{\odot}$
(1)	(2)	(3)	(4)	(5)	(6)	(7)	(8)	(9)
UGC1281	0.99	53.80	2.55	7.37	0.1078	0.3010	12.18	10.54
UGC1501	1.32	50.20	3.74	8.55	0.1813	0.3034	14.14	10.00
UGC5427	0.38	54.00	0.71	2.85	0.0091	0.1796	4.71	9.43
UGC7559	0.88	37.40	2.18	3.16	0.0834	0.3010	5.23	12.02
UGC8837	1.55	47.60	4.63	9.03	0.2236	0.3063	14.93	9.98
UGC7047	0.57	37.00	1.22	2.01	0.0281	0.2855	3.32	4.81
UGC5272	1.28	55.00	3.59	9.95	0.1730	0.3030	16.46	41.47
DDO52	1.30	60.00	3.66	12.03	0.1772	0.3032	19.89	22.29
DDO101	0.94	58.80	2.38	8.35	0.0965	0.3010	13.81	4.59
DDO154	0.75	38.00	1.76	2.78	0.0571	0.3003	4.60	32.24
DDO168	0.83	60.00	2.02	7.68	0.0729	0.3009	12.70	25.19
Haro29	0.28	32.60	0.47	0.76	0.0038	0.0851	1.26	5.29
Haro36	0.97	56.50	2.48	7.96	0.1033	0.3010	13.16	15.58
IC10	0.38	41.00	0.71	1.64	0.0091	0.1796	2.71	3.34
NGC2366	1.28	55.00	3.59	9.95	0.1730	0.3030	16.46	9.77
WLM	0.55	33.00	1.17	1.54	0.0255	0.2806	2.55	14.43
UGC7603	1.11	60.30	2.97	10.37	0.1352	0.3012	17.15	5.39
UGC7861	0.62	61.00	1.37	5.93	0.0352	0.2936	9.80	1.66
NGC1560	1.10	56.10	2.93	8.90	0.1329	0.3011	14.71	8.34
DDO125	0.49	17.00	1.00	0.36	0.0186	0.2583	0.60	1.32
UGC5423	0.52	39.50	1.08	2.09	0.0219	0.2711	3.45	3.79
UGC7866	0.54	28.70	1.14	1.14	0.0243	0.2778	1.89	3.39
DDO43	0.57	35.30	1.22	1.83	0.0281	0.2855	3.02	20.76
IC1613	0.60	19.00	1.31	0.56	0.0322	0.2909	0.92	2.16
UGC4483	0.16	20.80	0.22	0.18	0.0007	0.0133	0.29	8.20
KK246	0.58	34.60	1.25	1.78	0.0295	0.2875	2.95	13.41
NGC6822	0.56	35.00	1.19	1.76	0.0268	0.2832	2.92	3.89
UGC7916	1.63	37.00	4.95	5.74	0.2357	0.3073	9.48	41.15
UGC5918	1.23	45.00	3.40	6.40	0.1622	0.3024	10.59	14.13
AndIV	0.48	32.20	0.97	1.28	0.0176	0.2532	2.12	34.57
UGC7232	0.21	37.00	0.32	0.74	0.0016	0.0344	1.22	4.25
DDO133	0.90	42.40	2.25	4.16	0.0877	0.3010	6.88	10.93
UGC8508	0.28	25.50	0.47	0.47	0.0038	0.0851	0.77	6.05
UGC2455	1.06	47.00	2.79	6.02	0.1238	0.3011	9.95	1.44
NGC3741	0.18	23.60	0.26	0.26	0.0010	0.0202	0.43	4.95
UGC11583	0.17	52.20	0.24	1.19	0.0009	0.0165	1.97	6.30

TABLE IX. Mass model parameters of the LSB bin 1 galaxies.

Name	$a_d$ kpc	$v_{\text{opt}}$ km/s	$r_c$ kpc	$M_d$ $10^7 M_\odot$	$M_h(R_{\text{opt}})$ $10^{10} M_\odot$	$M_{\text{vir}}$ $10^{10} M_\odot$	$M/L$ $M_\odot/L_\odot$
(1)	(2)	(3)	(4)	(5)	(6)	(7)	(8)
UGC4115	0.40	24.20	0.76	4.01	0.0034	0.1187	439.35
F563V1	2.40	27.32	8.29	30.64	0.3881	0.7780	160.80
UGC11583	0.31	27.94	0.54	4.14	0.0016	0.0499	103.98
UGC2684	0.80	36.68	1.92	18.41	0.0258	0.6181	609.63
F574-2	4.47	40.00	18.98	122.33	0.7303	0.8193	193.89
F565V2	2.00	45.18	6.50	69.83	0.2732	0.7709	839.54
UGC5272	1.20	48.80	3.29	48.88	0.0794	0.7639	644.38
UGC8837	1.20	49.64	3.29	50.58	0.0794	0.7639	265.44
F561-1	3.60	50.85	14.23	159.22	0.6493	0.8011	209.90
UGC3174	1.00	51.68	2.58	45.68	0.0484	0.7328	239.75
NGC4455	0.90	53.00	2.25	43.24	0.0361	0.6908	75.15
UGC1281	1.70	55.00	5.24	87.96	0.1905	0.7700	291.27
UGC1551	2.52	55.80	8.85	134.21	0.4215	0.7802	17.69

- [1] P. J. E. Peebles, Large-scale background temperature and mass fluctuations due to scale-invariant primeval perturbations, *Astrophys. J. Lett.* **263**, L1 (1982).
- [2] S. D. White, C. S. Frenk, M. Davis, and G. Efstathiou, Clusters, filaments, and voids in a universe dominated by cold dark matter, *Astrophys. J.* **313**, 505 (1987).
- [3] A. Klypin, A. V. Kravtsov, O. Valenzuela, and F. Prada, Where are the missing galactic satellites?, *Astrophys. J.* **522**, 82 (1999).
- [4] B. Moore, S. Ghigna, F. Governato, G. Lake, T. Quinn, J. Stadel, and P. Tozzi, Dark matter substructure within galactic halos, *Astrophys. J.* **524**, L19 (1999).
- [5] D. Clowe, M. Bradač, A. H. González, M. Markevitch, S. W. Randall, C. Jones, and D. Zaritsky, A direct empirical proof of the existence of dark matter, *Astrophys. J. Lett.* **648**, L109 (2006).
- [6] S. J. Penny, C. J. Conselice, S. De Rijcke, and E. V. Held, Hubble space telescope survey of the perseus cluster–I. The structure and dark matter content of cluster dwarf spheroidals, *Mon. Not. R. Astron. Soc.* **393**, 1054 (2009).
- [7] J. S. Bullock and M. Boylan-Kolchin, Small-scale challenges to the  $\Lambda$ cdm paradigm, *Annu. Rev. Astron. Astrophys.* **55** (2017).
- [8] J. F. Navarro, C. S. Frenk, and S. D. M. White, A universal density profile from hierarchical clustering, *Astrophys. J.* **490**, 493 (1997).
- [9] J. M. Gaskins, A review of indirect searches for particle dark matter, *Contemp. Phys.* **57**, 496 (2016).
- [10] T. Matos, F. S. Guzmán, and L. A. Ureña López, Scalar field as dark matter in the universe, *Classical Quantum Gravity* **17**, 1707 (2000).
- [11] T. Matos and L. A. Ureña López, Quintessence and scalar dark matter in the universe, *Classical Quantum Gravity* **17**, L75 (2000).
- [12] T. Matos and L. A. Ureña López, Further analysis of a cosmological model with quintessence and scalar dark matter, *Phys. Rev. D* **63**, 063506 (2001).
- [13] V. Sahni and L. Wang, New cosmological model of quintessence and dark matter, *Phys. Rev. D* **62**, 103517 (2000).
- [14] W. Hu, R. Barkana, and A. Gruzinov, Fuzzy cold dark matter: The wave properties of ultralight particles, *Phys. Rev. Lett.* **85**, 1158 (2000).
- [15] A. Arbey, J. Lesgourgues, and P. Salati, Quintessential halos around galaxies, *Phys. Rev. D* **64**, 123528 (2001).
- [16] A. Arbey, J. Lesgourgues, and P. Salati, Cosmological constraints on quintessential halos, *Phys. Rev. D* **65**, 083514 (2002).
- [17] A. Arbey, J. Lesgourgues, and P. Salati, Galactic halos of fluid dark matter, *Phys. Rev. D* **68**, 023511 (2003).
- [18] S.-J. Sin, Late-time phase transition and the galactic halo as a Bose liquid, *Phys. Rev. D* **50**, 3650 (1994).
- [19] S. Ji and S.-J. Sin, Late-time phase transition and the galactic halo as a Bose liquid. II. The effect of visible matter, *Phys. Rev. D* **50**, 3655 (1994).
- [20] F. S. Guzmán, T. Matos, and H. Villegas, Scalar fields as dark matter in spiral galaxies: Comparison with experiments, *Astron. Nachr.* **320**, 97 (1999).
- [21] F. S. Guzmán and T. Matos, Scalar fields as dark matter in spiral galaxies, *Classical Quantum Gravity* **17**, L9 (2000).
- [22] J. Magaña and T. Matos, A brief review of the scalar field dark matter model, *J. Phys. Conf. Ser.* **378**, 012012 (2012).
- [23] A. Suárez, V. H. Robles, and T. Matos, A review on the scalar field/Bose-Einstein condensate dark matter model, in *Accelerated Cosmic Expansion* (Springer, New York, 2014), pp. 107–142.
- [24] T. Rindler-Daller and P. R. Shapiro, Complex scalar field dark matter on galactic scales, *Mod. Phys. Lett. A* **29**, 1430002 (2014).
- [25] D. J. Marsh, Axion cosmology, *Phys. Rep.* **643**, 1 (2016).



- [26] J. C. Niemeyer, Small-scale structure of fuzzy and axion-like dark matter, *Prog. Part. Nucl. Phys.* **113**, 103787 (2020).
- [27] T. Matos, L. A. Ureña López, and J.-W. Lee, Short review of the main achievements of the scalar field, fuzzy, ultralight, wave, BEC dark matter model, *Front. Astron. Space Sci.* **11**, 1347518 (2024).
- [28] H.-Y. Schive, T. Chiueh, and T. Broadhurst, Cosmic structure as the quantum interference of a coherent dark wave, *Nat. Phys.* **10**, 496 (2014).
- [29] C. Boehmer and T. Harko, Can dark matter be a Bose–Einstein condensate?, *J. Cosmol. Astropart. Phys.* **06** (2007) 025.
- [30] M. Membrado, A. Pacheco, and J. Sañudo, Hartree solutions for the self-Yukawian boson sphere, *Phys. Rev. A* **39**, 4207 (1989).
- [31] D. J. Marsh and P. G. Ferreira, Ultralight scalar fields and the growth of structure in the universe, *Phys. Rev. D* **82**, 103528 (2010).
- [32] H.-Y. Schive, M.-H. Liao, T.-P. Woo, S.-K. Wong, T. Chiueh, T. Broadhurst, and W. P. Hwang, Understanding the core-halo relation of quantum wave dark matter from 3d simulations, *Phys. Rev. Lett.* **113**, 261302 (2014).
- [33] B. Schwabe, J. C. Niemeyer, and J. F. Engels, Simulations of solitonic core mergers in ultralight axion dark matter cosmologies, *Phys. Rev. D* **94**, 043513 (2016).
- [34] J. Veltmaat and J. C. Niemeyer, Cosmological particle-in-cell simulations with ultralight axion dark matter, *Phys. Rev. D* **94**, 123523 (2016).
- [35] P. Mocz, M. Vogelsberger, V. H. Robles, J. Zavala, M. Boylan-Kolchin, A. Fialkov, and L. Hernquist, Galaxy formation with BECDM–I. Turbulence and relaxation of idealized haloes, *Mon. Not. R. Astron. Soc.* **471**, 4559 (2017).
- [36] D. Levkov, A. Panin, and I. Tkachev, Gravitational Bose-Einstein condensation in the kinetic regime, *Phys. Rev. Lett.* **121**, 151301 (2018).
- [37] P.-H. Chavanis, Mass-radius relation of newtonian self-gravitating Bose-Einstein condensates with short-range interactions. I. Analytical results, *Phys. Rev. D* **84**, 043531 (2011).
- [38] D. J. Marsh and A.-R. Pop, Axion dark matter, solitons and the cusp–core problem, *Mon. Not. R. Astron. Soc.* **451**, 2479 (2015).
- [39] S.-R. Chen, H.-Y. Schive, and T. Chiueh, Jeans analysis for dwarf spheroidal galaxies in wave dark matter, *Mon. Not. R. Astron. Soc.* **468**, 1338 (2017).
- [40] L. E. Padilla, J. Solís-López, T. Matos, and A. Áviléz-López, Consequences for the scalar field dark matter model from the McGaugh observed-baryon acceleration correlation, *Astrophys. J.* **909**, 162 (2021).
- [41] L. E. Padilla, T. Rindler-Daller, P. R. Shapiro, T. Matos, and J. A. Vázquez, Core-halo mass relation in scalar field dark matter models and its consequences for the formation of supermassive black holes, *Phys. Rev. D* **103**, 063012 (2021).
- [42] M. Mina, D. F. Mota, and H. A. Winther, Solitons in the dark: Non-linear structure formation with fuzzy dark matter, *Astron. Astrophys.* **662**, A29 (2022).
- [43] A. A. Avilez, L. E. Padilla, T. Bernal-Marin, and T. Matos, On the possibility that ultra-light boson haloes host and form supermassive black holes, *Mon. Not. R. Astron. Soc.* **477**, 3257 (2018).
- [44] S. May and V. Springel, Structure formation in large-volume cosmological simulations of fuzzy dark matter: Impact of the non-linear dynamics, *Mon. Not. R. Astron. Soc.* **506**, 2603 (2021).
- [45] T. Matos and L. A. Ureña-López, Flat rotation curves in scalar field galaxy halos, *Gen. Relativ. Gravit.* **39**, 1279 (2007).
- [46] F. S. Guzmán and L. A. Ureña López, Gravitational atoms: General framework for the construction of multistate axially symmetric solutions of the Schrödinger-Poisson system, *Phys. Rev. D* **101**, 081302 (2020).
- [47] L. A. Ureña López and A. Bernal, Bosonic gas as a galactic dark matter halo, *Phys. Rev. D* **82**, 123535 (2010).
- [48] M. Alcubierre, J. Barranco, A. Bernal, J. Degollado, A. Diez-Tejedor, M. Megevand, and O. Sarbach, I-boson stars, *Classical Quantum Gravity* **35**, 08 (2018).
- [49] E. W. Kolb and M. S. Turner, Limits to the radiative decays of neutrinos and axions from-pray observations of SN 1987a (1987).
- [50] F. Dalfovo, S. Giorgini, L. P. Pitaevskii, and S. Stringari, Theory of Bose-Einstein condensation in trapped gases, *Rev. Mod. Phys.* **71**, 463 (1999).
- [51] B. Li, T. Rindler-Daller, and P. R. Shapiro, Cosmological constraints on Bose-Einstein-condensed scalar field dark matter, *Phys. Rev. D* **89**, 083536 (2014).
- [52] A. Suárez and P.-H. Chavanis, Cosmological evolution of a complex scalar field with repulsive or attractive self-interaction, *Phys. Rev. D* **95**, 063515 (2017).
- [53] P. R. Shapiro, T. Dawoodbhoy, and T. Rindler-Daller, Cosmological structure formation in scalar field dark matter with repulsive self-interaction: The incredible shrinking Jeans mass, *Mon. Not. R. Astron. Soc.* **509**, 145 (2021).
- [54] E. Castellanos and T. Matos, Klein-Gordon fields and Bose-Einstein condensates: Thermal bath contributions, *Int. J. Mod. Phys. B* **27**, 1350060 (2013).
- [55] V. H. Robles and T. Matos, Exact solution to finite temperature SFDM: Natural cores without feedback, *Astrophys. J.* **763**, 19 (2013).
- [56] T. Matos, E. Castellanos, and A. Suárez, Bose–Einstein condensation and symmetry breaking of a complex charged scalar field, *Eur. Phys. J. C* **77**, 500 (2017).
- [57] E. Armengaud, N. Palanque-Delabrouille, C. Yèche, D. J. E. Marsh, and J. Baur, Constraining the mass of light bosonic dark matter using SDSS Lyman- $\alpha$  forest, *Mon. Not. R. Astron. Soc.* **471**, 4606 (2017).
- [58] F. S. Guzmán and L. A. Ureña López, Gravitational atoms: General framework for the construction of multistate axially symmetric solutions of the Schrödinger-Poisson system, *Phys. Rev. D* **101**, 081302 (2020).
- [59] M. Persic, P. Salucci, and F. Stel, The universal rotation curve of spiral galaxies—I. The dark matter connection, *Mon. Not. R. Astron. Soc.* **281**, 27 (1996).
- [60] P. Salucci, A. Lapi, C. Tonini, G. Gentile, I. Yegorova, and U. Klein, The universal rotation curve of spiral galaxies—II. The dark matter distribution out to the virial radius, *Mon. Not. R. Astron. Soc.* **378**, 41 (2007).
- [61] C. Di Paolo, P. Salucci, and A. Erkurt, The universal rotation curve of low surface brightness galaxies—IV. The interrelation

- between dark and luminous matter, *Mon. Not. R. Astron. Soc.* **490**, 5451 (2019).
- [62] E. V. Karukes and P. Salucci, The universal rotation curve of dwarf disc galaxies, *Mon. Not. R. Astron. Soc.* **465**, 4703 (2016).
- [63] C. D. Paolo, P. Salucci, and J. P. Fontaine, The radial acceleration relation (RAR): Crucial cases of dwarf disks and low-surface-brightness galaxies, *Astrophys. J.* **873**, 106 (2019).
- [64] F. S. Guzmán and L. A. Ureña López, Evolution of the Schrödinger-Newton system for a self-gravitating scalar field, *Phys. Rev. D* **69**, 124033 (2004).
- [65] E. Seidel and W.-M. Suen, Formation of solitonic stars through gravitational cooling, *Phys. Rev. Lett.* **72**, 2516 (1994).
- [66] F. S. Guzman and L. A. Urena-Lopez, Gravitational cooling of self-gravitating Bose-condensates, *Astrophys. J.* **645**, 814 (2006).
- [67] I. D. Karachentsev, D. I. Makarov, and E. I. Kaisina, Updated nearby galaxy catalog, *Astron. J.* **145**, 101 (2013).
- [68] K. C. Freeman, On the disks of spiral and S0 galaxies, *Astrophys. J.* **160**, 811 (1970).
- [69] L. E. Padilla, L. O. Tellez, L. A. Escamilla, and J. A. Vazquez, Cosmological parameter inference with Bayesian statistics, *Universe* **7**, 213 (2021).
- [70] M. Newville, T. Stensitzki, D. B. Allen, and A. Ingargiola, LMFIT: Non-linear least-square minimization and curve-fitting for Python, 2014.
- [71] D. Foreman-Mackey, D. W. Hogg, D. Lang, and J. Goodman, emcee: The MCMC hammer, *Publ. Astron. Soc. Pac.* **125**, 306 (2013).
- [72] F. Guzmán and A. A. Ávilez, Head-on collision of multistate ultralight boson dark matter configurations, *Phys. Rev. D* **97**, 116003 (2018).
- [73] J. Solís-López, F. S. Guzmán, T. Matos, V. H. Robles, and L. A. Ureña López, Scalar field dark matter as an alternative explanation for the anisotropic distribution of satellite galaxies, *Phys. Rev. D* **103**, 083535 (2021).
- [74] B. P. Moster, R. S. Somerville, C. Maulbetsch, F. C. van den Bosch, A. V. Macciò, T. Naab, and L. Oser, Constraints on the relationship between stellar mass and halo mass at low and high redshift, *Astrophys. J.* **710**, 903 (2010).
- [75] F. Donato, G. Gentile, P. Salucci, C. Frigerio Martins, M. I. Wilkinson, G. Gilmore, E. K. Grebel, A. Koch, and R. Wyse, A constant dark matter halo surface density in galaxies, *Mon. Not. R. Astron. Soc.* **397**, 1169 (2009).
- [76] L. A. Ureña López, V. H. Robles, and T. Matos, Mass discrepancy-acceleration relation: A universal maximum dark matter acceleration and implications for the ultralight scalar dark matter model, *Phys. Rev. D* **96**, 043005 (2017).
- [77] A. D. Cintio, C. B. Brook, A. A. Dutton, A. V. Macciò, G. S. Stinson, and A. Knebe, A mass-dependent density profile for dark matter haloes including the influence of galaxy formation, *Mon. Not. R. Astron. Soc.* **441**, 2986 (2014).
- [78] <http://www.iac.edu.mx>.
- [79] <https://clusterhibrido.cinvestav.mx/>.